International Journal of Applied Earth Observation and Geoinformation 146 (2026) 105162

Contents lists available at ScienceDirect

International Journal of Applied Earth Observation and Geoinformation

journal homepage: www.elsevier.com/locate/jag

Analysis of the 4 December 2021 lahar on Mount Semeru using optical and SAR remote sensing

Samuel McGowan [a,*], Jonathan Procter [a], Gabor Kereszturi [a], Fabien Albino [b], Indranova Suhendro [c]

[a] Volcanic Risk Solutions, Institute of Agriculture and Environment, Massey University, Private Bag 11222, Palmerston North, 4442, New Zealand
[b] Institut des Sciences de la Terre (ISTerre), Universite Grenoble Alpes, Universite Savoie Mont Blanc, France
[c] Department of Environmental Geography, Faculty of Geography, Universitas Gadjah Mada, 10 Sekip Utara, Yogyakarta, 55281, Indonesia

ARTICLE INFO

Keywords:
Mount Semeru
Lahar
SAR
Amplitude change detection
Supervised classification

ABSTRACT

This study characterizes the amplitude changes associated with the 4 December 2021 eruption of Mount Semeru and maps the resulting deposits using Sentinel-1 SAR backscatter and PlanetScope optical imagery. Results show that lahar deposits caused surface smoothening which reduced SAR backscatter, whereas pyroclastic density currents (PDCs) increased backscatter due to higher moisture content. We have also shown the potential of differential polarimetric responses between surface cover types to identify areas of channel widening and vegetation destruction, providing a rapid means of identifying impacted areas in the context of volcanic crisis management. The supervised classification of SAR and high-resolution optical images enabled the production of an accurate geomorphological map able to separate different pyroclastic flow and lahar flow deposits both sedimentologically and spatially. Classified channelized lahar deposits were also used to quantify channel widening associated with the eruption, which significantly impacted the Supiturang Village.

1. Introduction

Mount Semeru is one of the world's most prolific producers of lahars, generating more than 5 large scale lahars (> 5,000,000 m^3) since 1884, with small to medium lahars (≤ 0.1 million m^3) occurring weekly during the rainy season (Solikhin et al. 2012). Lahars are mixtures of water and pyroclastic material originating on steep volcanic slope (Waitt, 2013) and can be produced during (primary) or after an eruption (secondary) following strong precipitation (e.g., Mount Pinatubo, Philippines, 1991; Mount Semeru, Indonesia, 2021), through crater lake eruptions (e.g., Ruapehu, New Zealand, 2007), or by interaction of snow and ice with volcanic hot material (e.g., Nevado del Ruiz, Colombia, 1985) (Schilling, 2014). Lahars at Mount Semeru are predominantly classified as hyperconcentrated flows (water-dominated and turbulent mixtures), driven by the continuous supply of remobilizable volcanic material stored on steep unvegetated upper slopes, combined with periods of heavy rainfall (Dumaisnil et al., 2010; Procter et al., 2021). These flows are particularly destructive due to overbanking and avulsion processes, as channels located southeast of the edifice are wide with little incision, causing rapid stream infilling and bank inundation, placing human installations and agricultural fields at considerable risk (Thouret et al., 2007) (Fig. 1). Over 10,000 lahar-related casualties have been reported in the twentieth century (Thouret et al., 2007). The surrounding ring plain is home to more than one million people, with major cities including Malang (600,000 people, 35 km west) and Lumajang (85,000 people, 33 km east). Agriculture, plantations and forestry production are the main economic activities in the surrounding ring plain, favoured by nutrient-rich volcanic soils that support high agricultural production (Rozaki et al., 2022; Shoji and Takahashi, 2002). Mount Semeru's continuous sediment supply also provides valuable construction material through sand and stone mining in the channels (Irawan et al., 2024; Rozaki et al., 2022). Despite mitigation constructions (e.g., dams and dikes) and hazard mapping (e.g., Volcanological Survey of Indonesia 1986 and 1992; Siswowidjoyo et al., 1997; Thouret et al., 2007; Irawan et al., 2024), neighbouring communities remain highly exposed to PDCs and lahars due to continuous volcanic activity and high population density in disaster-prone areas (Wahyuningtyas et al., 2021). Among the most exposed communities is Supiturang Village, located along the upper Besuk Kobokan channel (Fig. 1a). The village lies on the southeastern flank of Mount Semeru, directly downstream of the main eruptive vent and within the main lahar and PDC pathway. At the time of writing of this article, Mount Semeru produced a large eruption on 19 November 2025, generating a series of PDCs travelling up to 13 km SE, leading

* Corresponding author.
E-mail address: s.mcgowan@massey.ac.nz (S. McGowan).

https://doi.org/10.1016/j.jag.2026.105162
Received 17 November 2025; Received in revised form 26 January 2026; Accepted 7 February 2026
Available online 12 February 2026

to the evacuation of about 1116 people (Global Volcanism Program, 2025). Mount Semeru thus exemplifies the complex balance between socio-economic activities while being significantly exposed to the impacts of hazardous volcanic phenomena. Given these risks, effective hazard management during volcanic crises is essential to rapidly detect impacted areas and support decision-making during an event. Remote sensing has become a central tool for mapping and monitoring lahar deposits and associated geomorphic change, particularly in regions where access during or after an eruption is limited. Optical imagery, such as Landsat, Sentinel-2, ASTER, SPOT, UAVs and PlanetScope (Roy et al., 2021; Macorps et al., 2023), has been widely used to delineate lahar footprints, channel avulsion and overbank deposition based on spectral contrasts and textural information (Joyce et al., 2009; Solikhin et al., 2015b; Andrade et al., 2022). However, optical remote sensing is hampered by cloud cover, ash/steam plumes and vegetation cover which are common in tropical volcanic environments. Radar remote sensing, and in particular Synthetic Aperture Radar (SAR), overcomes these limitations by acquiring large-scale data at day or night independently of cloud cover, making it particularly advantageous for monitoring tropical volcanic regions such as Indonesia (Pallister et al., 2013; Pepe and Calò, 2017). SAR images contain an information of phase and amplitude of the backscatter signal. On one hand, Interferometry Synthetic Aperture Radar (InSAR) uses combination of phase difference calculated between two epochs for deriving time series of surface displacements maps, which supports the monitoring of volcanic unrest (Ezquerro et al., 2023; Bemelmans et al., 2023; Wang et al., 2024; Wei et al., 2024; Orynbaikyzy et al., 2025; Popescu et al., 2025). On the other hand, time series of SAR amplitude images provide relevant information on surfaces changes. Such changes could be due to the evolution of the surface itself (new deposits, appearance/destruction of forest/buildings) or the changes in the surface's properties (roughness or moisture content). For this reason, changes in backscatter amplitude has been extensively used on active volcanoes to map lava flow, pyroclastic density currents (PDCs), lahars and debris avalanches (Wadge et al., 2011; Solikhin et al., 2015a; Albino et al., 2020; Dualeh et al., 2021; Poland, 2022; Ezquerro et al., 2023; Ferrentino et al., 2023; Lee et al., 2023; Orynbaikyzy et al., 2023). Despite the recognized potential of satellite remote sensing for lahar hazard management, its operational use remains limited by constraints in sensor availability, revisit times, and delays in image acquisition and dissemination (Kerle and Oppenheimer, 2002). While SAR sensors can overcome cloud-related limitations, their effective use during volcanic crisis requires careful data processing and interpretation guided by knowledge of surface scattering mechanisms and land cover conditions. In contrast, cloud-free high-resolution optical imagery provides direct visual evidence of surface changes, but is constrained by weather conditions, vegetation cover or ash clouds. Therefore, combining both approaches leverages the all-weather capability of SAR and the direct interpretability of optical data, enabling accurate surface mapping. In this context, this study presents an integrated SAR-optical workflow to map surface changes and volcanic deposits associated with the 4 December 2021 eruption at Mount Semeru along the Besuk Kobokan channel. By combining Sentinel-1 SAR backscatter images and polarimetric response analysis with high resolution PlanetScope optical imager (Fig. 1c), we demonstrate how impacted areas and geomorphic change can be rapidly identified and classified. This approach provides a practical process chain for emergency response and hazard monitoring, without relying on complete ground-based observations, and is transferrable to other data-limited, rapidly evolving tropical volcanic environments.

2. Case study: 4 december 2021 eruption and lahar at Mount Semeru

Eruptions at Mount Semeru have been ongoing since 2014, but between March and December 2021, activity increased notably, with daily seismic events interpreted as eruptions (Global Volcanism Program, 2022). The 4 December 2021 eruption was triggered by pressure release following lava dome collapse in the Jonggring-Seloko crater, exacerbated by strong erosion from heavy rainfall in November (555 mm accumulated) (Cahyadi et al., 2024; Suhadha and Harintaka, 2024). Lava dome collapses began on 1 December, with the largest event occurring on 4 December, producing lava flows and PDCs that travelled up to 16 km towards the southeast, destroying numerous roads and bridges such as the Gladak Perak bridge (Fig. 1b), located 13 km from the summit (Global Volcanism Program, 2022; Kristianto et al., 2023). A significant ash cloud rose to 15 km, causing sudden darkness and depositing ash across Lumajang and Malang regencies, leading to roof collapses (Fig. 2e). Ash deposition combined with heavy rainfall favoured lahar generation, with the total estimated volume of the December 4 lahar being approximately 6 million m^3 (Hendrawan et al., 2023). According to Indonesia's regional disaster management agency report (Badan Penanggulangan Bencana Daerah, 2021), the eruption resulted in 48 fatalities, damage or destruction of 1027 residential houses, more than 3000 animals killed, and the evacuation of 10,565 people accommodated across 151 refugee centers. In response, the Indonesian Government prohibited all human activity within a 1 km radius of the volcano, extending this restriction to 5 km in the southeastern section. Consequently, seven disaster-prone villages in the Pronojiwo and Candipuro sub-districts were permanently relocated, with their residents accommodated in 1951 shelter units (International Federation of Red Cross and Red Crescent Societies, 2022). Field observations showed that the PDCs were initially hot but rapidly transitioned into cold and wet flows due to heavy rainfall (around 15 mm/h), as evidenced by accretionary lapilli, unsinged trees and wooden and plastic materials (Suhendro et al., 2025). The primary PDC deposit was characterized by angular to subrounded fragments mainly originating from the collapsed dome (vesicular-black and porphyritic (V-BP), dense-grey and porphyritic (D-GP), dense-grey and highly porphyritic (D-GhP)), with some accidental lithics (vesicular-reddish and weakly porphyritic (V-RwP)) (Suhendro et al., 2025). This deposit was poorly sorted with the largest blocks reaching 75 cm and the matrix composed of coarse ash (Fig. 2c). Gas escaping from the top of the PDC deposits were observed during field visits on 7 December 2021 (Fig. 2b). The overlying lahar deposits showed evidence of imbrication of large fragments (maximum size of 30 cm) and was poorly sorted with subangular to rounded clasts within a sandy matrix (medium sand) that lacked fines (Fig. 2a). This deposit exhibited much more heterogeneous fragments compared to the primary PDC deposit and did not show evidence of gas escapes. The overbank lahar facies was also poorly sorted but dominated by medium-fine sand with smaller maximum fragment sizes (< 25 cm) and significantly greater heterogeneity, including older volcanic products (Fig. 2f). Secondary lahars incising through the PDC and primary lahar deposits (Fig. 2c) revealed 4–5 m thick deposition of newly emplaced material associated with the 4 December 2021 eruption (Perwita et al., 2023)(Fig. 2d). The secondary cutting lahars carry smaller grain sizes with a maximum fragment size of 15 cm, and a fine-sand or silt matrix. Subangular to rounded fragments are typically heterogeneous with a greater presence of older products.

3. Dataset and methodology

3.1. Synthetic Aperture Radar (SAR)

Interferometry Synthetic Aperture radar (InSAR) is commonly used to study volcanic deformation (e.g., Albino and Biggs, 2021; Lundgren et al., 2017) and to generate DEMs (Kubanek et al., 2015; McAlpin and Meyer, 2013) following a volcanic event using the phase component of a SAR image. The phase-based deformation techniques are of limited use in tropical vegetated areas due to loss of coherence due to temporal and geometrical decorrelation (e.g., atmospheric artefacts, steep slopes) (Ebmeier et al., 2013). Amplitude (amount of signal

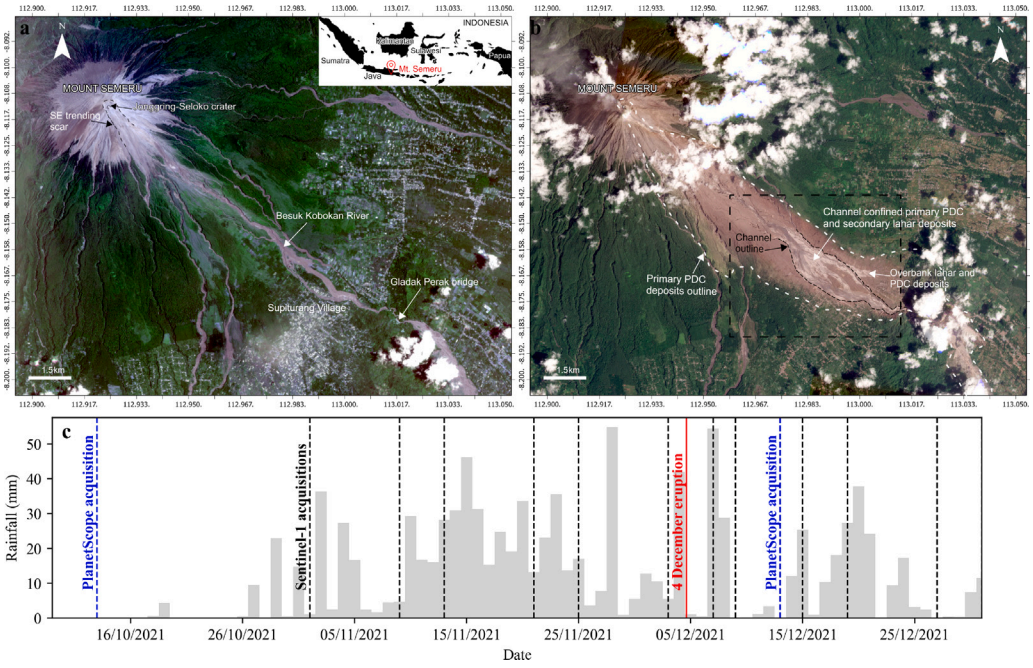

Fig. 1. PlanetScope images acquired at Mount Semeru (a) pre-eruption (13/10/2021) and (b) post-eruption (13/12/2021) showing the impact of the 04/12/2021 lahar. (c) Daily rainfall data acquired from GSMaP data overlaid by acquisition dates for Sentinel-1 (black dashed lines) and PlanetScope images (blue dashed lines) used in this study relative to the 4/12/2021 eruption (red line).

backscattered by an object towards the sensor) retrieved from multi-temporal SAR image analysis are suitable for mapping surface deposits and landscape evolution, as changes in scatterer distribution and properties will affect the amount of backscattering (Solikhin et al., 2015a). Amplitude is often expressed in decibels due to the high dynamic range of radar backscatter (Dualeh et al., 2021). The factors controlling radar amplitude backscattering are the specifications of the acquisition (wavelength, incidence angle, polarization, spatial resolution and orbit path) and the illuminated surface properties (surface roughness, dielectric properties, topography, water content) (Ezquerro et al., 2023; Meyer, 2019). Surfaces facing towards the sensors produce a strong return signal while slopes facing away produce little return. Smooth flat surfaces such as water also produce low signal return therefore appearing darker in the image, while dry or rough surfaces diffuse the backscattering in multiple directions generating a strong return appearing bright in the image. In steep environments, shadowing effects also produce no return signal in slopes facing away from the sensor. Pixels appear differently according to the polarization of the acquisition, for example vegetation has a strong depolarization effect due to volumetric scattering which will appear darker in co-polarized images and brighter in cross-polarized images (Kellndorfer et al., 2019; Meyer, 2019; Solikhin et al., 2015a). However, for mapping volcanic products, there is no general agreement on which polarization is better suited (Dualeh et al., 2021; Solikhin et al., 2015a). Tracking lahars is often challenging with SAR backscattering analysis because multiple flow events of varying magnitude can occur between image acquisitions (Macorps et al., 2023). The distinct imprint of the December 2021 lahar, together with the dense temporal coverage of Sentinel-1, therefore presents the ideal case study for testing the capability of SAR to detect and monitor lahar-related surface change.

3.2. Sentinel-1 IW SLC dataset and processing steps

This study investigates Sentinel-1 (C-band, $\lambda = 5.6$ cm) Interferometric Wide (IW) Single Look Complex (SLC) images from both the ascending and descending orbit to generate backscatter images. Sentinel-1 has a revisit cycle of 6 days and acquires data in single (HH, VV) or dual polarization (HH+HV, VV+VH) with an incidence angle ranging between 29.1° and 173.46°. De Zan and Monti Guarnieri (2006). A single IW swath covers a width of 250 km with a 5 × 20 m spatial resolution, sub-divided into three sub-swaths and individual bursts were used. We used the Sentinel Application Platform (SNAP) to process our SAR data and QGIS for visualization and interpretation of results. To be able to compare amplitude images from different sensors, modes, or orbits, SAR images need to be calibrated (Freeman, 1992). There are three common calibration methods, defined as Beta (β^0), Sigma (σ^0), and Gamma (γ^0). Radar backscatter (β) describes the ratio between the scattered power ρ_s and incident power ρ_i ($\mathrm{W\,m^{-2}}$) (Small, 2011). For a pixel area A_β, the radar brightness (β^0) is defined by:

$$\beta^0 = \frac{\beta}{A_\beta} \tag{1}$$

This normalization does not require knowledge of the local incidence angle. The proportion of backscattering corrected for the incidence angle (θ_i) and the distance between the target and the sensor is described as the Radar Cross Section (RCS, σ). For a pixel surface area A_σ, this is expressed as:

$$\sigma^0 = \beta^0 \cdot \frac{A_\beta}{A_\sigma} = \beta^0 \sin\theta_i \tag{2}$$

Where σ^0 is the normalized RCS for a single pixel (Small, 2011). To combine and compare images acquired from both Sentinel-1 orbits, which have different incidence angles, we use the Gamma (γ) backscattering coefficient (Small, 2011). This method also considers local topography by using a DEM to remove radiometric variations induced by slopes facing towards or away from the sensor, while preserving radiometric variability associated with different land covers (Meyer et al., 2015). We use the 30 m resolution Copernicus DEM to perform this radiometric correction, defined as:

$$\gamma_r^0(r,a) = K_r \cdot \frac{\beta^0(r,a)}{\hat{A}_\gamma(r,a)} \tag{3}$$

Where r and a are the range and azimuth image coordinates, K_r is a scalar calibration constant, and $\hat{A}_\gamma(r,a)$ represents the simulated local illuminated area in the radar geometry (Small, 2011). The Copernicus

Fig. 2. Field photographs showing (a) overlying lahar deposit, (b) evidence of gas escape process in PDC deposits, (c) outcrop showing the relationship between the dome collapse PDC deposits with lahars deposits, (d) side view of the outcrop showing destruction of vegetation on channel banks (humans for scale dressed in orange), (e) house damaged by the PDCs and (f) lahar overbank deposits. Blue arrows indicate the downstream direction of the channel. Location of photographs seen in Fig. 6a. Photographs acquired on 07/12/2021 by Suhendro.I.

DEM is also used to remove the geometrical distortions induced by local topography such as layover and foreshortening present in SAR images. Shadow areas, where the slope angle is higher than the incidence angle, cannot be retrieved. The complete SNAP processing workflow is highlighted in Fig. 3a. All products are subset to focus on Mount Semeru and the upper section of the Besuk Kobokan river located SE of the crater, and coregistered using the earliest acquisition as a reference (01/11/2021) to obtain sub-pixel alignment accuracy between each image.

3.3. Surface mapping

3.3.1. SAR backscattering analysis

SAR amplitude analysis was used previously for volcanic applications such as lava mapping (Arnold et al., 2019; Ezquerro et al., 2023; Lee et al., 2023), dome evolution (Grémion et al., 2023; Kubanek et al., 2015; Pallister et al., 2013; Wang et al., 2015), PDCs and lahars (Dualeh et al., 2021; Kurnianto et al., 2024; Solikhin et al., 2015a; Wadge et al., 2011). There are various methods in which to quantify and visualize changes in amplitude such as computing the ratio or difference between successive dates (Arnold et al., 2018; Goitom et al., 2015; Wadge et al., 2002), and by composite RGB representations (Dualeh et al., 2021; Ezquerro et al., 2023; Wadge et al., 2011). We assign the first amplitude image to the red channel, the second amplitude image to the green channel and the difference between the second image and the first in the blue channel (Fig. 3b).

This visualization method displays unchanged areas in yellow, areas which have increased in amplitude in the second image appear blue and areas which have decreased in amplitude in the second image appear red. This variation in amplitude reflects changes in surface roughness and/or moisture content: smoother or wetter surfaces tend to decrease backscatter, whereas rougher or drier surfaces lead to an increase. The Rayleigh criterion, defined as $h > \lambda/(8\cos(\theta))$, is commonly used to determine a material size threshold above which pixels appear rough, or below which they appear smooth in SAR amplitude images. Here, h represents the ground's height variation, λ is the acquisition wavelength, and θ is the incidence angle (Dualeh et al., 2021). In our study, objects with height variations below 0.77 cm ($\lambda = 5.6$ cm, $\theta = 36°$) will therefore appear smooth in the SAR images.

3.3.2. Supervised classification of surface deposits

To support our SAR surface mapping, we select two PlanetScope Scene Surface reflectance images acquired by the SuperDove instrument (PSB.SD) to perform supervised Random Forest classifications. The images from by this generation of satellites are composed of 4 bands (Blue, Green, Red and Near-Infrared) with a 3 m pixel resolution and near daily acquisitions (Roy et al., 2021). Random Forest Classification uses multiple decision trees and applies a majority voting rule to assign each observation to a class (Breiman, 2001). This algorithm can deal with large number of input features and avoids overfitting making it a trusted and robust classification algorithm (Billah et al., 2023; Du et al., 2015; Lee et al., 2024). For both classification, Region of Interests

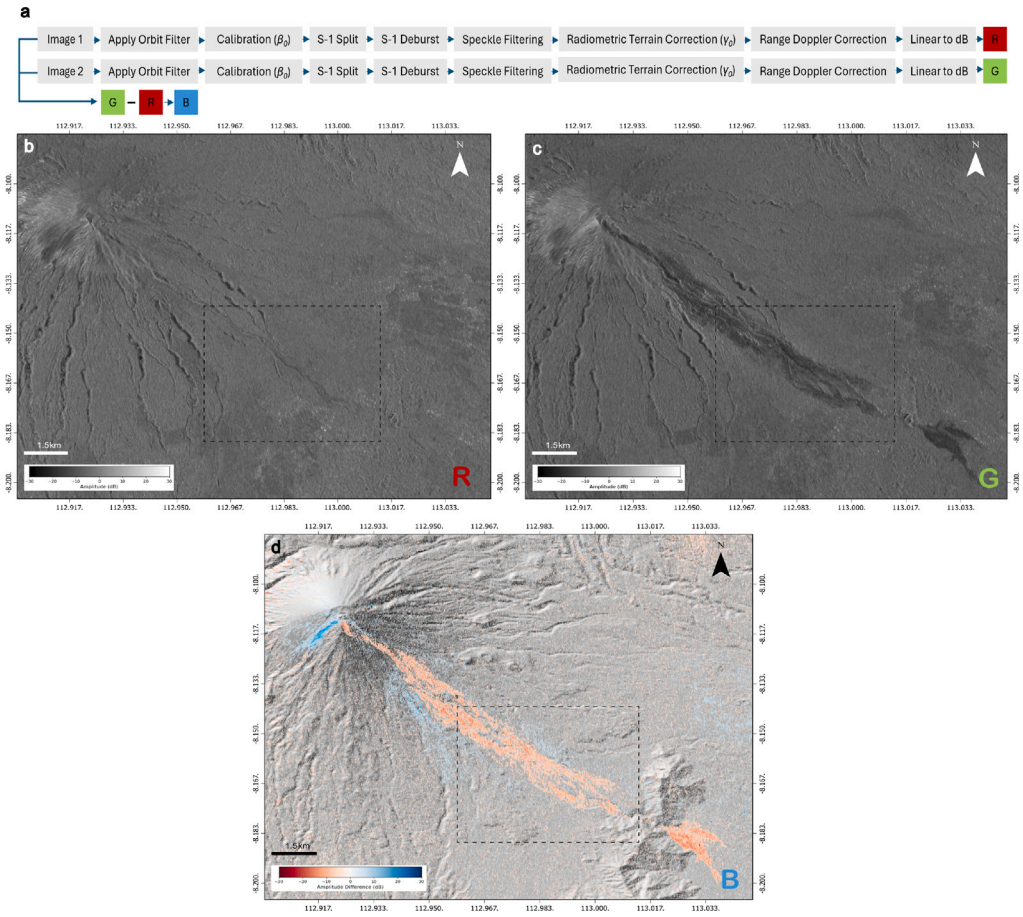

Fig. 3. (a) SNAP workflow used to produce corrected and calibrated Sentinel-1 backscatter images to integrate in RGB amplitude change difference maps where (b) the pre-eruption image is placed in the red channel, (c) the post-eruption image in the green channel and (d) the amplitude difference between the post- and pre-image in the blue channel. SAR images are coregistered using the earliest date beforehand to ensure pixel alignment. We use the 30 m Copernicus DEM used to correct geometric and radiometric distortions.

Table 1
List of bands and indexes used to perform our post-eruption supervised classification. PlanetScope bands have been normalized to correct for scene-to-scene differences.

Sensor	Variables	Bands	Reference
Sentinel-1	Amplitude change detection (VV, VH)	R: 25/11/2025 G: 07/12/2021 B: G - B	Dualeh et al. (2021) Macorps et al. (2023) Solikhin et al. (2015a)
	Coherence (VV, VH)	25/11/2021 and 07/12/2021	Poland (2022) Solikhin et al. (2015a)
PlanetScope Scene	Red (650–680 nm) Green (547–585 nm) Blue (465–515 nm)	RGB	Tan et al. (2021)
	Near Infrared (845–885 nm)	NIR	Tan et al. (2021)
	Normalized Difference Vegetation Index (NDVI)	$\frac{\text{NIR} - R}{\text{NIR} + R}$	Pettorelli (2013)
	Normalized Difference Water Index (NDWI)	$\frac{G - \text{NIR}}{G + \text{NIR}}$	Gao (1996)
	Enhanced Vegetation Index (EVI)	$\frac{G \times (\text{NIR} - R)}{\text{NIR} + C_1 \times R - C_2 \times B + L}$	Bannari et al. (1995)
	Brightness Index (BI)	$\sqrt{\frac{R^2 + G^2 + B^2}{3}}$	Richardson and Wiegand (1977)
	Intensity (I)	$\frac{R + G + B}{3}$	Shih and Liu (2005)

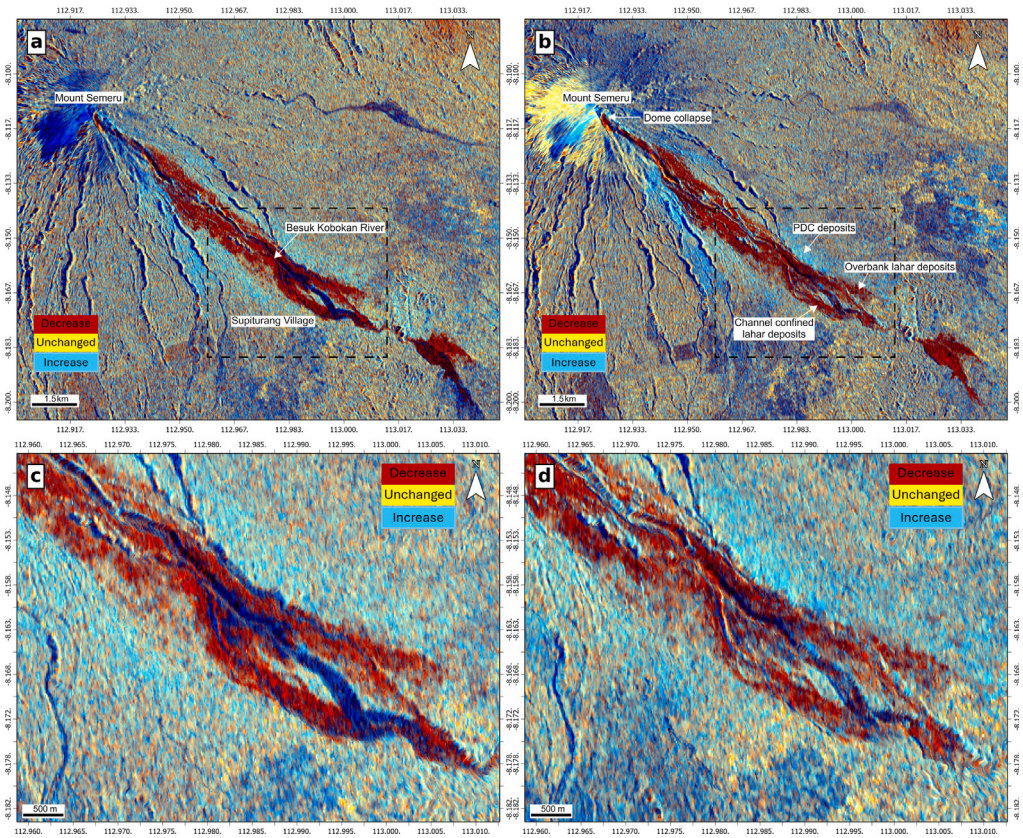

Fig. 4. Sentinel-1 amplitude change images of the 04/12/2021 Mount Semeru eruption using 25/11/2021 as pre-eruption image (Red band), 07/12/2021 as post-eruption (Green band), and the difference post-pre (Blue band) for both a-(c) VH and b-(d) VV polarization. Positive post-pre differences (blue colour) indicate increased backscatter relative to pre-eruptive conditions (rougher/wetter surfaces), negative differences (red colour) indicate decreased backscatter (smoother/drier surfaces), and near-zero differences (yellow colour) indicate unchanged surfaces. Dotted black box in (a) and (b) represents location of insets (c) and (d). Images acquired from the ascending pass.

(ROIs) are digitized in QGIS and are randomly divided into training (80%) and validation (20%) (Fig. A.1). We first use a pre-eruption image acquired on the 13 October 2021 to delineate river channels prior to the eruption. This scene was selected as the nearest cloud-free pre-eruption scene, with minimal geomorphic change expected before early December. The image was divided into two classes called channel and non-channel, where river channels are clearly identifiable by their distinct darker colour, which contrasts clearly with surrounding vegetation. These polygons are later used to digitize and quantify geomorphic changes associated with the December 2021 eruption (channel outline used in Fig. 5). This first classification relies exclusively on PlanetScope data. An image acquired on 13 December 2021 has low cloud coverage allowing us to study the impact of the lahar on the SE ring plain. We define seven surface types based on optical visual interpretation and SAR-derived surface characteristics. Table 1 summarizes the variables selected to perform the post-eruption classification to best separate geological and non-geological ring-plain classes.

4. Results

4.1. Amplitude change detection

Our analysis concentrates on the SE ring plain affected by the 4th of December lahar and PDCs, therefore ignoring amplitude variations observed near the crater related to dome collapse and distal variations related to potential ash fall. For both polarizations, we observe amplitude increase (blue colour in Fig. 4) on either side of the Besuk Kobokan river. We attribute this increase to PDC tephra deposition and heavy rainfall (Suhendro et al., 2025), which increases soil moisture retention and consequently enhances SAR backscatter, particularly in co-polarization (Kellndorfer et al., 2019). Although dry ash deposition may locally smooth the surface and reduce backscatter amplitude, the observed signal increase is interpreted relative to the pre-eruption surface and reflects wetter near-surface conditions at the time of the post-eruption acquisition. Field evidence indicates that rainfall intensities (15 mm/h) rapidly cooled the PDCs, producing wet deposits rather than dry ash layers, thereby increasing the dielectric contrast at C-band Suhendro et al. (2025), Verhoest et al. (2008). We also suggest that the destruction of vegetation (branches, leaves) by the passage of the PDC may also lead to stronger double-bounce scattering mechanism, which is more sensitive for VV than VH polarization (Meyer, 2019). We do not observe any amplitude increase within the channel generally associated with emplacement of block-and-ash flows (BAFs) (Dualeh et al., 2021; Suhendro et al., 2025; Wadge et al., 2011), likely due to masking by overlying fine-grained lahar deposits emplaced subsequently. Lahar deposits emplaced in the channel and in overbank areas lead to a decrease in amplitude for both polarizations (red pixels in Fig. 4), indicative of a reduction in surface roughness on the scale of C-band radar wavelength (5.6 cm). Field analysis of overbank-facies show a rare occurrence of large blocks, with deposits consisting exclusively of ash-sized materials (Suhendro et al., 2025), consistent with a reduction in surface roughness. However, we do observe slight differences in intensities of amplitude decrease according to the polarization used. For example, the delineation of vegetation destruction in overbanks and for channel retreat is sharper in the VH polarization (Fig. 4c) than for VV polarization (Fig. 4d). The intensity of amplitude decrease in the central channel branch is stronger for VV polarization (brighter red colour in Fig. 4d) than for VH polarization

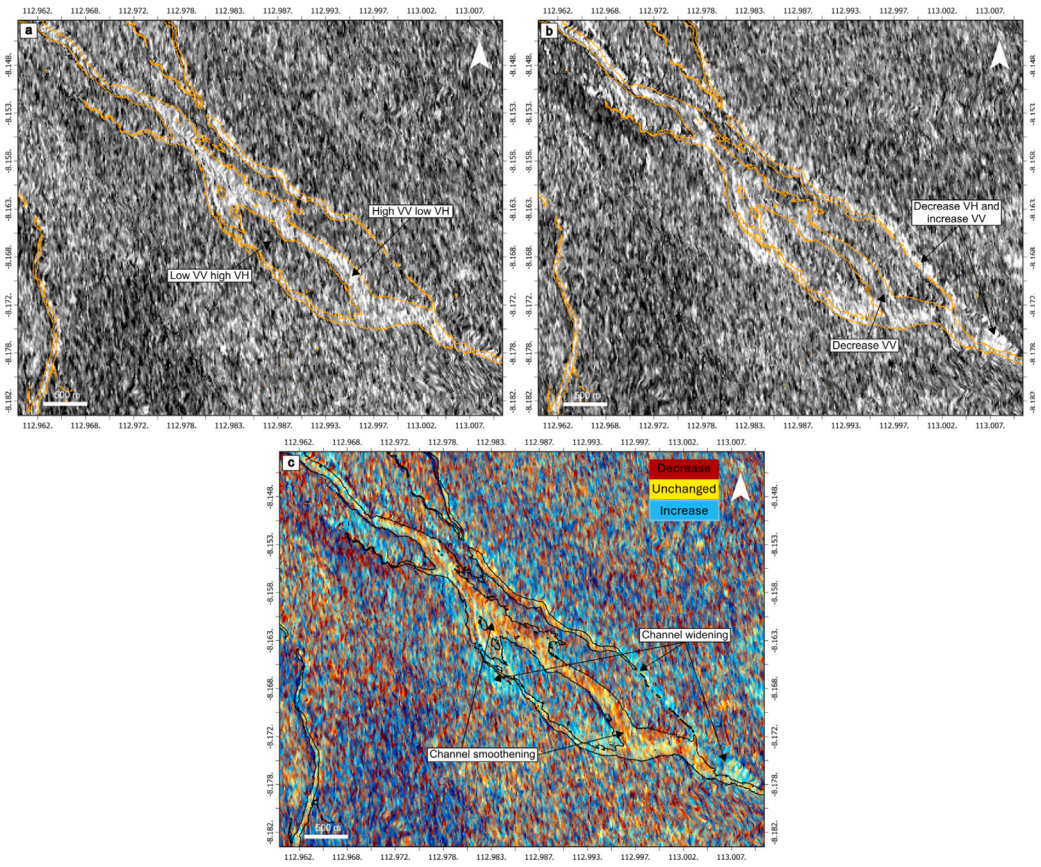

Fig. 5. VV-VH amplitude difference computed (a) pre-eruption (25/11/2021) and (b) post-eruption (07/12/2021) and combined into a RGB image placing the pre-eruption image in the red channel, the post-eruption in the green channel and the difference between the post-and-pre-eruption in the blue channel. Brown and black line represents the pre-eruption channel outline (see Section 4.3).

(red-dark blue colour in Fig. 4c). The VV/VH ratio (or VV-VH when expressed in dB), is commonly used in SAR analysis to enhance the discrimination of surface scattering mechanisms (Phan et al., 2021; Soudani et al., 2021), as VV polarization is more sensitive to surface roughness and double bounce scattering (wave interaction between two surfaces normal to each other such as the ground and vertical structures), while VH responds strongly to volumetric scatterers such as vegetation with higher backscattering (Meyer, 2019). Analysis of the VV-VH difference images before (Fig. 5a) and after the eruption (Fig. 5b) highlights clear contrasts in scattering mechanism with bright pixels representing areas of low VH and/or strong VV backscattering, and inversely for darker pixels. Channels, being largely vegetation-free for both acquisitions, appear with consistently bright VV-VH responses due to low volumetric VH backscattering and stronger VV backscattering. Channel widening and vegetation destruction is expressed as new bright areas (reduction in VH) in previously dark zones (Fig. 5a and b) and correspond to blue pixels in the RGB composite (Fig. 5c). In contrast, pre-existing channels infilled by lahar deposits transition from bright to darker pixels (Fig. 5a and b) or appear as red in the RGB composite (Fig. 5c), reflecting reduced VV backscattering due to surface smoothing. Overbank lahar and PDC deposits are more difficult to delineate using VV-VH, as multiple scattering processes occurring within partially damaged vegetation and urban environments and are better identified when computing amplitude differences for each polarization pre-and post-eruption (Fig. 4). Variations in VV-VH polarimetric responses clarify differences in backscatter change intensity observed in Fig. 4 for identical surface covers, highlighting the influence of polarization on the SAR signal.

4.2. Surface deposit classification

Our supervised classification of the PlanetScope Image acquired on 13 December 2021 and derived SAR products enabled the creation of a detailed map of the deposits associated with the 4 December lahar (Fig. 6a). Deposits are classified into non-geological classes (vegetation, fields, urbanization) and geological classes (PDC deposits, channelized lahar deposits, lahar overbank). The geological classes are defined based on visual interpretation of optical imagery, considering both the textural and colour characteristics of the deposits as well as their spatial context (channelized versus overbank settings). The amplitude change associated with these overbank deposits is also considered to further separate PDC from lahar deposits as they induce an increase and decrease in backscatter respectively. The channelized lahar deposits are divided into water-saturated and dry sediments, where the darker colour indicates water-saturated material within actively flowing braided streams, while the dry deposits correspond to lighter, flattened channel bars where sediments have dried. Overbank class represents deposition of lahar sediments outside of the main channel, with their emplacement generally restricted to < 700 m from the channel margins. Integrating elevation data, such as a post-eruption DEM, into the supervised classification could improve the separability of these classes by using variables such as slope angle, topographic position index and evolution in channel position. We did not integrate the pre-eruption DEM as part of the lahar deposits now occur in areas located outside of the pre-existing channels and would therefore induce misclassification.

Among these classes, the water-saturated channelized lahar deposits are the most frequently misclassified because of their similarity to other surface types (Table 2). It is particularly misclassified as overbank

Table 2
Confusion matrix for 13 December 2021 PlanetScope Image.

	Predicted class								
	Class	Vegetation	Fields	Urban	PDC	Dry lahardeposits	Water-saturatedlahar deposits	Overbanklahar	Total
True class	Vegetation	**1433**	0	0	0	0	66	0	1499
	Fields	0	**613**	0	0	0	19	0	632
	Urban	0	0	**83**	0	0	61	0	144
	PDC	0	1	0	**1072**	0	709	0	1782
	Dry lahar deposits	0	0	0	0	**413**	324	0	737
	Water-saturatedlahar deposits	0	0	0	0	5	**2966**	5	2976
	Overbanklahar	0	0	0	0	0	2202	**2081**	4283
	Total	1433	614	83	1072	418	6347	2086	12053
	Accuracy	F1-score = 0.72							

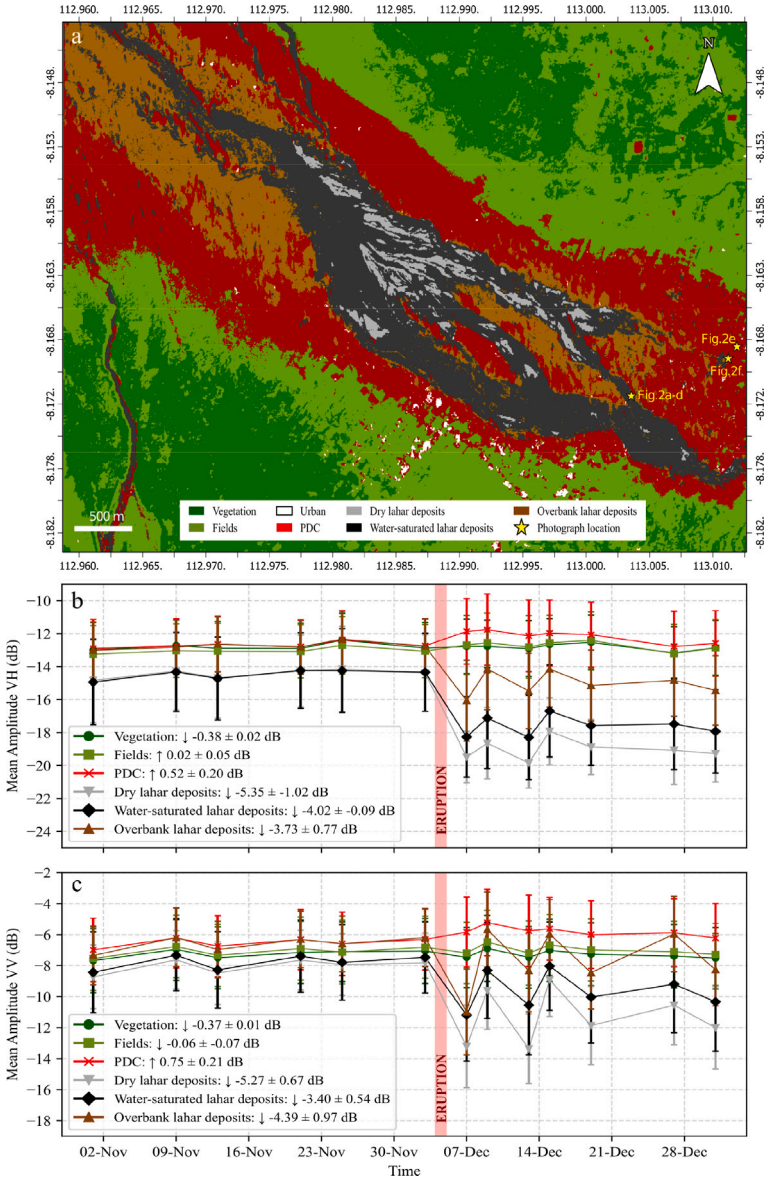

Fig. 6. (a) Map of deposits emplaced following the 4 December eruption at Mount Semeru based on the supervised classification of PlanetScope and SAR images, and their associated mean amplitude extracted through time for both (b) VH and (c) VV polarization. For each class, the mean radar backscatter was calculated by averaging the amplitude of all pixels assigned to that class in each Sentinel-1 acquisition, allowing temporal changes to be tracked per class. The urban class was removed for amplitude extraction. Values of amplitude change associated with each class (shown in the legend of b) and (c) were obtained by differencing Sentinel-1 images acquired on 07/12/2021 and 25/11/2021, representing the changes attributed with the eruption.

lahar deposits as both exhibit a decrease in amplitude and typical low reflectance areas. It also contains isolated pixels distributed across other classes (i.e., "salt and pepper" effect). To address this, majority filter was applied with a size of a 3 × 3 pixels, as a post-classification refinement. This filtering replaces each pixel's class with the most frequently occurring class within a 3 × 3 neighbourhood window,

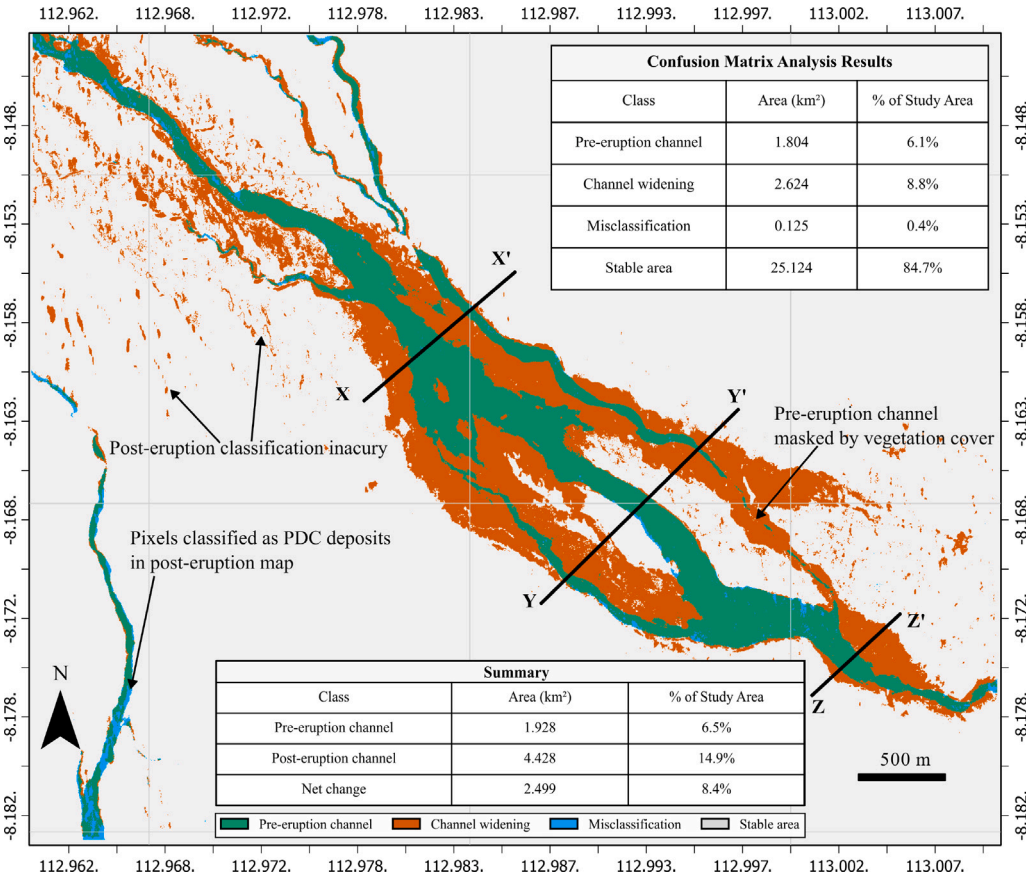

Fig. 7. Confusion matrix showing channel evolution following 4 December 2021 eruption, by comparing pre- and post-eruption channel extents. The post-eruption channel is derived by merging channelized lahar classes from Fig. 6. Solid black lines represent cross section profiles used in Fig. 9. Solid black lines represent cross section profiles used in Figs. 8 and 9.

effectively removing isolated misclassification while preserving genuine class boundaries. To evaluate the improvement, the confusion matrix was recomputed using the same independent validation dataset used during model validation (Fig. A.2). Results show that the original classification contains numerous isolated misclassified pixels scattered throughout the image. The filtering changed approximately 2.25% of total pixels, with most changes occurring at class transition zones. The overall accuracy increases with F1-score improving from 0.72 to 0.84, and the channelized water-saturated lahar deposits recall decreasing from 56% to 72%. The filtered classification produced more spatially coherent clusters that better reflect the continuous nature of lahar deposit units. This filtering exercise was conducted solely to demonstrate the spatial distribution of misclassified pixels and validate the classification performance. All subsequent analyses and interpretations presented in this study utilized the original unfiltered classification to preserve the model's direct predictions.

This surface mapping provides a basis for monitoring backscatter evolution over time across different surface types and for quantifying the mean amplitude change associated with the December 4th deposits. The strongest mean amplitude decrease for both polarizations is observed for the dry lahar deposits (VH: −5.35 dB, VV: −5.27 dB) (Fig. 6b and (c), caused by the surface smoothening in the channel. The mean amplitude decrease associated with the water-saturated lahar deposits is of a slightly lower magnitude (VH: −4.02 dB, VV: −3.40 dB), also due to surface smoothening, but moderated by higher moisture content present within the sediments that increases backscattering. In VH polarization (Fig. 6b), channelized water-saturated lahar deposits show larger mean amplitude decrease (−4.02 dB) than the overbank lahar deposits (−3.73 dB). This is due to the removal and burial of vegetated areas associated with channel widening and lahar emplacement. The destruction of the vegetated banks eliminates the strong volumetric scattering mechanisms that originally characterized these areas, resulting in greater VH amplitude reduction. Conversely, in VV polarization (Fig. 6c), overbank lahar deposits experienced larger amplitude reduction (−4.39 dB) compared to channelized water-saturated lahar deposits (−3.40 dB). This pattern indicates that the pre-eruption overbank areas, comprising of fields, forests, urban infrastructures, possessed rougher surfaces and strong double bounce scattering, generating stronger VV backscatter. The surface smoothening and the destruction force induced by the overbanking reduces the contribution of these scatterers, resulting in a greater VV amplitude reduction. This also confirms that the surface roughness conditions in the pre-eruption channel decreased as well, but to a lesser extent than in overbank areas.

4.3. Channel evolution

By merging the channelized lahar classes (dry and water-saturated) obtained from the post-eruption classification (Fig. 6a), a new channel geomorphology of the Besuk Kobokan river is derived (Fig. 7). We use a confusion matrix analysis to compare pre-and post-eruption binary channel classifications and assess changes in channel footprint (Fig. 7). In this framework, green pixels represent the pre-eruption channel, orange pixels indicate channel widening post-eruption, blue pixels denote areas classified as channel only in the pre-eruption map (often due to post-eruption misclassification), and grey pixels indicate stable non-channel areas. Using the pixel resolution of the produced map (3 × 3 m), we compute surface area change relative to the extent of the site of study. Therefore, values retrieved do not represent the overall surface change associated with the 4 December 2021 eruption,

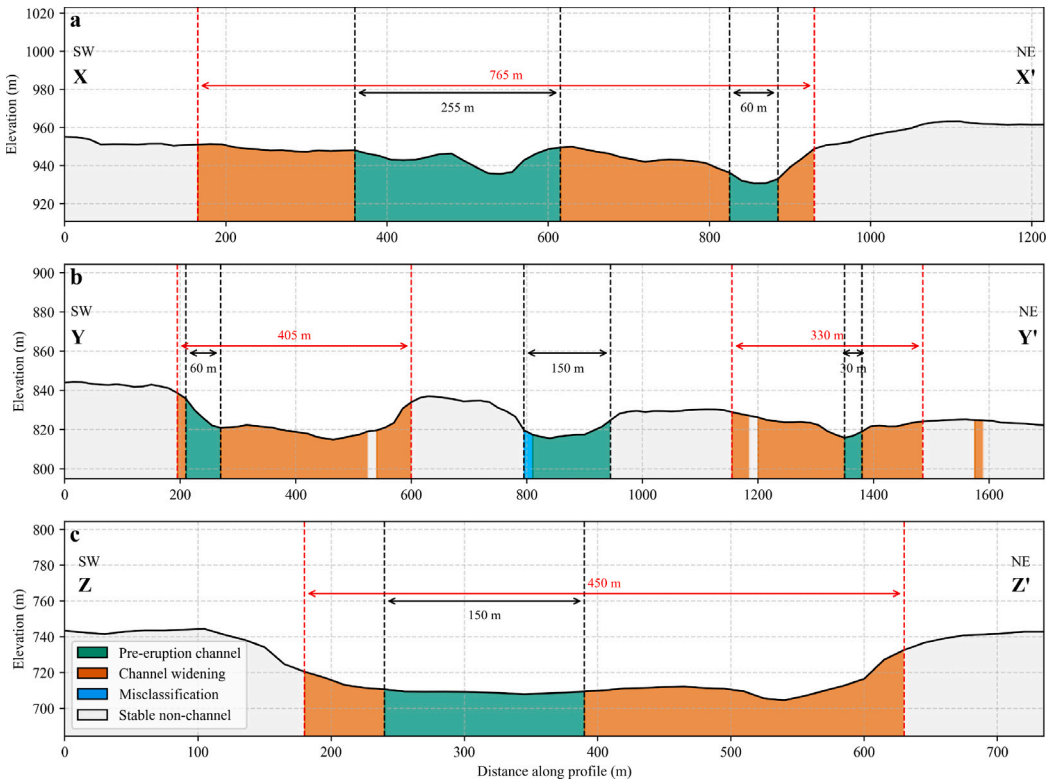

Fig. 8. Cross section profiles of the Besuk Kobokan river showing evolution in channel width following the 4 December 2021 lahar. Location of cross section profiles is in Fig. 7. Topography extracted using the DEMNAS DEM. Note that the pre-eruption channel extent may not fully coincide with the topography due to temporal evolution between DEM acquisition (2018) and classifications (2021), and potential interpolation effects.

but rather the surface change in the vicinity of the Supiturang Village, where geomorphological change was the largest. Our results show that the pre-eruption channel covered 1.928 km^2, a value that we expected to be slightly underestimated due to narrow channel segments masked by overlaying vegetation canopy and limited spatial resolution (Fig. 7). The post-eruption channel extends over 4.428 km^2, representing an apparent increase of 2.499 km^2. This increase is likely overestimated because of pixels in overbank areas being identified as channel in the post-eruption map. The low misclassified area (0.125 km^2, 0.4% of study area) indicates that almost all pre-eruption channel segments were successfully captured in the post-eruption map. Most misclassified pixels arise from areas within the true channel that were identified as PDC or overbank lahar deposits, rather than representing omissions of entire channel segments. This confirms that the post-eruption surface classification (Fig. 6a) reliably identified the main channel network, providing a solid basis for assessing channel widening. Cross section profiles extracted along different portions of the channel provide a vertical perspective on geomorphic change (Fig. 8). The elevation data is extracted from the 8 m resolution DEMNAS multi DEM (TerraSAR-X, IFSAR, ALOS PALSAR and mass point) which we resampled to 15 m for consistency with the other classification datasets (Iswari and Anggraini, 2018; Julzarika and Harintaka, 2019). This DEM was selected not only for its finer spatial resolution compared to the 30 m Copernicus DEM, but also because it is the most recent open-access DEM available for the area prior to the eruption (published in 2018). However, during this time gap we still expect changes to have occurred due to the frequent volcanic and lahar activity at Mount Semeru, as well as material anthropomorphic excavation. Consequently, the pre-eruption channels may have been shallower than represented, meaning that if we assume 4–5 m of lahar deposits for the December 2021 eruption, our observed overbanking and channel widening may not fully correspond to the actual post-eruption conditions. These profiles highlight areas susceptible to lateral geomorphic adjustment and overbanking. Profile X-X' illustrates the merging of two pre-eruption channels into a single 765 m-wide channel, with most lateral expansion occurring towards the southwest due to shallow topography and limited incision (Fig. 8a). The 60 m-wide northeastern channel is bordered by a steeper scarp that confines the flow within the channel bed. Portions of this bank may have been eroded and incorporated into the lahar, although this cannot be confirmed without post-elevation data. In section Y-Y', we note that the pre-eruption channel extent shows poor alignment with the topography for the narrow lateral channels due to interpolation effects and potential channel evolution since DEM acquisition in 2018. Additionally, we expect these channels to be wider than represented in profile b, as the spatial resolution of PlanetScope images combined with shadowing effects and vegetation cover can mask portions of the channel floor, preventing their identification as 'channel' in the pre-eruption classification. Despite these limitations, the pattern reverses from profile X-X': the northeastern branch (30 m-wide) exhibits limited incision and low-relief banks, favouring rapid aggradation and overbank deposition, while the western bank of the southwest channel (60 m) is steeper, with lateral migration primarily directed towards the northeast (Fig. 8b). The absence of lateral expansion in the central 150 m-wide channel suggests that flow energy was insufficient to drive significant bank erosion, with changes occurring primarily through vertical scour or deposition. The good alignment between both pre-and post-eruption channel positions and the 2018 topography supports this interpretation, though we acknowledge that some channel evolution may have occurred between 2018 and 2021 due to both ongoing lahar activity and anthropogenic excavation. Section Z-Z' shows the convergence of the three channel branches into a single constricted reach (150 m-wide), forming a bottleneck that likely enhance flow velocity, localized erosion and sediment accumulation (Fig. 8c). Part of this flat bottom channel was previously occupied by agriculture fields, which have been buried or eroded by the lahar widening the channel to 450 m. Optical imagery also reveals evidence of bank failure and slumping caused by basal undercutting from the lahar flow.

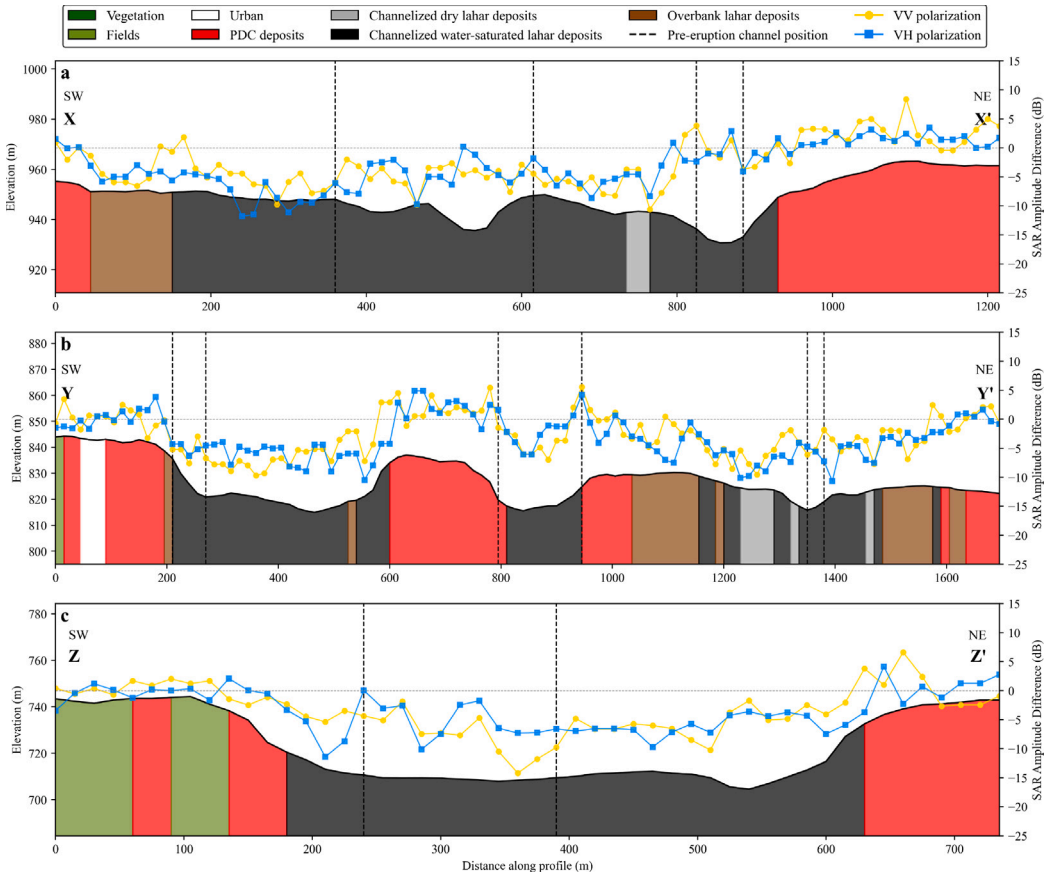

Fig. 9. Cross section profiles across the Besuk Kobokan river showing the surface deposits and amplitude change associated with the 4 December 2021 Mount Semeru eruption. Amplitude values are extracted for both polarizations using the difference between 07/12/2021 and 25/11/2021 Sentiel-1 images. Location of cross section profiles seen in Fig. 7. Topography extracted using the DEMNAS DEM. Extent of the new post-eruption channel is given by the channelized water-saturated and dry lahar deposits.

5. Discussion

5.1. Application SAR and optical imagery for mapping volcanic deposits

The combined use of Sentinel-1 SAR and high-resolution PlanetScope optical imagery provides an effective framework for mapping surface changes and deposits following the 4 December 2021 eruption of Mount Semeru. Sentinel-1 offers continuous temporal coverage under persistent cloud conditions and was particularly useful for distinguishing lahar deposits from PDCs. The backscatter response of the PDC deposits in overbank areas at Mount Semeru showed an increase in amplitude (Fig. 9), which we associate with an increase of moisture content of ash deposited in overbank areas due to heavy rainfall accompanying the eruption (Suhendro et al., 2025). Channelized and overbank lahar deposits exhibited a decrease in amplitude due to surface smoothening at the scale of C-band acquisition, with a stronger decrease observed for wetter dark channelized sediments (Fig. 9). These results are similar to observations following the 2010 Merapi eruption using L-band (λ = 23.6 cm) ALOS-PALSAR data, where valley-confined and overbank BAF deposits reduce amplitude, while pyroclastic-surge and tephra fall along BAF edges increases backscatter (Solikhin et al., 2015a). At Colima and Calbuco, L-band mapping combined with Landsat optical imagery indicated a decrease in amplitude following PDC and ash-cloud surge deposits, but an increase where lahars had eroded or re-exposed rough surfaces (Macorps et al., 2023). X-band (λ = 3.1 cm) and C-band (λ = 5.6 cm) observations of pyroclastic surge deposits at Soufriere Hills (TerraSAR-X) and Fuego (COSMO-SkyMed and Sentinel-1) showed a decrease in backscatter, with narrow bands of amplitude increase inside the main channels reflecting deposition of coarser BAF material (Dualeh et al., 2021; Wadge et al., 2011). These findings demonstrate that the same volcanic deposits can produce contrasting backscatter responses depending on radar wavelength, acquisition geometry, and local surface characteristics. The complex interplay between pre- and post-eruption surface conditions therefore limits the standalone interpretability of SAR data, reinforcing the value of integrating optical imagery and site-specific knowledge to refine geological discrimination and contextual interpretation. The integration of PlanetScope imagery augment spatial and spectral observations necessary to interpret lahar pathways and deposits. Combined with the SAR results, the high-resolution optical images allowed us to further distinguish channelized lahar deposits into two geological classes based on sediment colour, reflecting differences in moisture content and the presence of active streams. Identifying these active flow paths is crucial to indicate areas of ongoing sediment transport, channel incision and potential instability. These locations represent likely pathways for future lahars and zones where erosion may continue to modify the channel morphology, providing essential information for future hazard assessment, the installation of early-warning systems and the planning of monitoring and mitigation structures in downstream sectors. In addition, PlanetScope imagery enabled the separation of channel deposits from lahar overbank deposits, which SAR backscatter alone cannot reliably differentiate. This multi-sensor approach improved the mapping of the post-eruption geomorphology of the Besuk Kobokan river, allowing us to identify areas of channel widening and overbanking with greater confidence.

5.2. Limitations and implications for volcanic hazard monitoring

While the integration of Sentinel-1 and PlanetScope imagery proved highly effective for mapping the December 2021 eruption at Mount Semeru, several limitations remain. A key limitation to this approach lies in the spatial resolution and quality of the PlanetScope acquisition used for the pre-eruption classification, where narrow channels or vegetated channels be misclassified or partially obscured by canopy cover. Similarly, the post-eruption channel extent, derived from the supervised classification of volcanic deposits, is subject to uncertainty related to spectral overlap between geological classes. The absence of recent pre- and post-eruption elevation data further restricts our ability to quantify volumetric change (erosion and infilling), limiting the assessment to surface footprint. However, in our case given that both pre- and post-eruption classifications achieved high accuracy, these uncertainties are unlikely to significantly influence the overall interpretation of geomorphic change. Another important consideration is the temporal availability of cloud-free optical imagery, which in this case was exceptionally favourable. The rapid acquisition of PlanetScope imagery immediately after the event allowed detailed deposit mapping before any significant alteration, but in many tropical volcanic regions, persistent cloud cover may hinder optical observations during critical post-eruption periods. Under such circumstances, reliance on SAR data alone can limit the ability to discriminate between channelized and overbank deposits or to identify active flow paths. Nonetheless, the polarimetric assessment of Sentinel-1 data provided particularly useful for detecting zones of channel widening and lateral geomorphic change, as variations in polarization response highlighted contrasts between bare channel surfaces and vegetated channel margins. The differential polarimetric response between deposit types also reflects the distinct physical processes operating during lahar emplacement, with channel widening and infilling primarily destroying volumetric scatterers while overbank deposition primarily smoothens surface roughness. This polarization sensitivity offers potential for automated mapping of lahar impact zones and quantifying the relative contributions of erosional versus depositional processes in future volcanic hazard assessments. These contrasts enable rapid identification of channel modification even in the absence of post-eruption optical or elevation data, providing a valuable tool for volcanic crisis management. This approach performs best where vegetated banks or surfaces provide sufficient backscatter contrast to delineate geomorphic boundaries, making it particularly effective in tropical volcanic environments, such as Indonesia, but more limited on unvegetated volcanic ring plains. Successful application also requires SAR acquisitions with at least dual polarization. A further limitation to this approach is the spatial resolution of Sentinel-1, which may prevent the detection of narrow channels that higher resolution X-band sensors can capture, though these are often not openly accessible. An additional limitation arises from subsequent eruptive activity at Mount Semeru following the December 2021 event. Post-2021 activity includes eruptions in December 2022, and the major eruption of 19 November 2025. The latest major eruption produced extensive PDCs that deposited large volumes of pyroclastics along the SE flank, overlapping the drainage systems analysed in this study. Subsequent rainfall-driven remobilization of these deposits has generated lahars, although these are smaller than the 4 December 2021 lahar. The emplacement and remobilization of new pyroclastics likely altered channel morphology, sediment availability and distribution, surface roughness within the Besuk Kobokan catchment. As a result, the geomorphic configuration and lahar pathways documented here represent pre-2025 conditions and may differ substantially from the present-day landscape, highlighting the need for up-to-date SAR observations in such inherently dynamic volcanic landscapes. While this does not affect the validity of our interpretation of the 4 December 2021 lahar, it limits the direct transferability of mapped deposits and channel extents to current hazard assessments. Nevertheless, our results provide an important baseline for evaluating post-eruption landscape evolution and for assessing how PDC and lahar events progressively reshape lahar-prone channels at Mount Semeru.

6. Conclusion

By integrating Sentinel-1 SAR and PlanetScope optical imagery, this study effectively mapped lahar and pyroclastic deposits, quantified channel widening and distinguished surface scattering mechanisms associated with the 4 December 2021 eruption of Mount Semeru. The integration of multi-sensor datasets proved essential to overcome the limitations of individual methods, particularly in tropical environments where persistent cloud cover can restrict optical observations, and where the variable nature of SAR backscatter limits its standalone interpretability. Rapid identification of channel widening, lahar pathways, and overbank deposits using SAR offers crucial support for volcanic hazard assessment and emergency response planning, helping to locate potentially impacted communities. However, the effectiveness of this response depends on the temporal frequency and availability of SAR acquisitions. Our study also highlights the need for recurrent elevation mapping, particularly in fast-evolving landscapes such as tropical volcanic ring plains.

CRediT authorship contribution statement

Samuel McGowan: Writing – original draft, Visualization, Methodology, Investigation, Formal analysis, Data curation, Conceptualization. **Jonathan Procter:** Writing – review & editing, Supervision, Methodology, Funding acquisition, Conceptualization. **Gabor Kereszturi:** Writing – review & editing, Validation, Supervision, Methodology, Investigation. **Fabien Albino:** Writing – review & editing, Validation, Methodology. **Indranova Suhendro:** Writing – review & editing, Validation, Resources.

Declaration of competing interest

The authors declare that they have no known competing financial interests or personal relationships that could have appeared to influence the work reported in this paper.

Acknowledgements

This project is funded by the ‘Transitioning Taranaki to a Volcanic Future’ Research Programme of the Ministry of Business, Innovation and Employment’s Endeavour Fund. The authors also acknowledge the constructive comments and suggestions of three anonymous reviewers, which greatly improved the clarity and quality of the manuscript. The authors also thank Øystein Lund Andersen for generously sharing post-eruption drone imagery, which was invaluable for interpreting surface processes and validating geomorphic observations.

Appendix A. Supplementary data

See Figs. A.1 and A.2.

Appendix B. Supplementary data

Supplementary material related to this article can be found online at https://doi.org/10.1016/j.jag.2026.105162.

Data availability

Data will be made available on request.

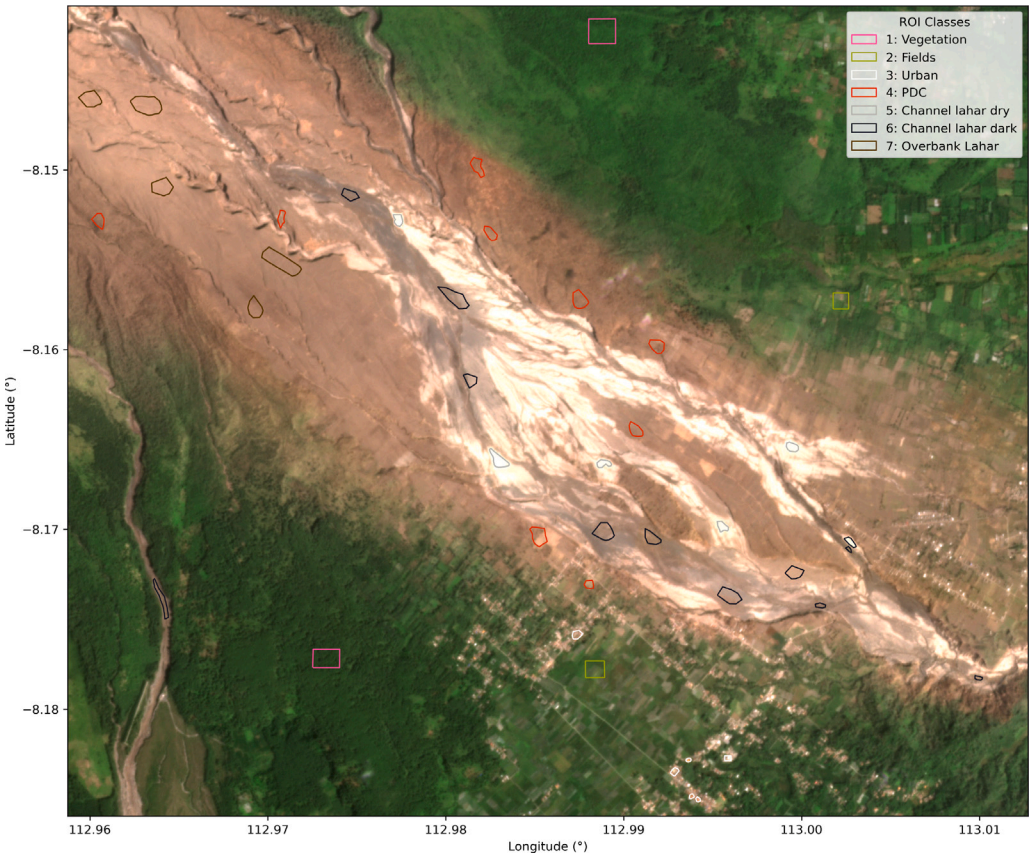

Fig. A.1. Location of ROIs digitized for our supervised classification.

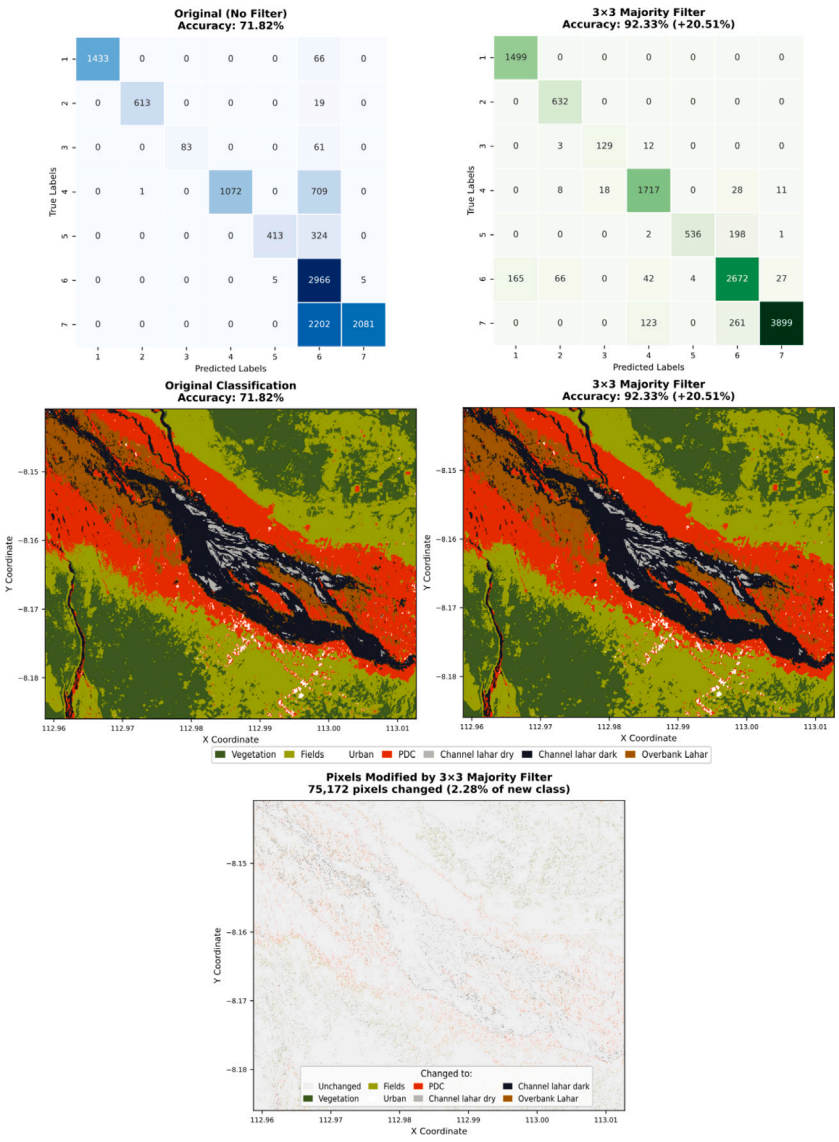

Fig. A.2. Comparison of original and majority filtered classification results. Confusion matrices (top), classified maps (middle), and spatial distribution of changed pixels (bottom) for original and 3 × 3 majority filtered classifications of the 13 December 2021 lahar deposits. Class numbers in confusion matrices follow the same order as Table 2 and the order of the caption located below the maps seen here.

References

Albino, F., Biggs, J., 2021. Magmatic processes in the east african rift system: Insights from a 2015–2020 sentinel-1 insar survey. Geochem. Geophys. Geosystems 22 (3), http://dx.doi.org/10.1029/2020GC009488.

Albino, F., Biggs, J., Escobar-Wolf, R., Naismith, A., Watson, M., Phillips, J.C., Marroquin, G.C., 2020. Using TanDEM-X to measure pyroclastic flow source location, thickness and volume: Application to the 3rd june 2018 eruption of fuego volcano, guatemala. J. Volcanol. Geotherm. Res. 406, 107063.

Andrade, S.D., Saltos, E., Nogales, V., Cruz, S., Lee, G., Barclay, J., 2022. Detailed cartography of cotopaxi's 1877 primary lahar deposits obtained by drone-imagery and field surveys in the proximal northern drainage. Remote. Sens. 14 (3), http://dx.doi.org/10.3390/rs14030631.

Arnold, D.W., Biggs, J., Dietterich, H.R., Vargas, S.V., Wadge, G., Mothes, P., 2019. Lava flow morphology at an erupting andesitic stratovolcano: a satellite perspective on El Reventador, Ecuador. J. Volcanol. Geotherm. Res. 372, 34–47. http://dx.doi.org/10.1016/j.jvolgeores.2019.01.009.

Arnold, D., Biggs, J., Wadge, G., Mothes, P., 2018. Using satellite radar amplitude imaging for monitoring syn-eruptive changes in surface morphology at an ice-capped stratovolcano. Remote Sens. Environ. 209, 480–488. http://dx.doi.org/10.1016/j.rse.2018.02.040.

Badan Penanggulangan Bencana Daerah, 2021. Update on the disaster management situation of mount semeru eruption.

Bannari, A., Morin, D., Bonn, F., Huete, A.R., 1995. A review of vegetation indices. Remote Sens. Rev. 13 (1–2), 95–120. http://dx.doi.org/10.1080/02757259509532298.

Bemelmans, M.J., Biggs, J., Poland, M., Wookey, J., Ebmeier, S., Diefenbach, A.K., Syahbana, D., 2023. High-resolution InSAR reveals localized pre-eruptive deformation inside the crater of Agung Volcano, Indonesia. J. Geophys. Res.: Solid Earth 128 (5), http://dx.doi.org/10.1029/2022JB025669.

Billah, M., Islam, A.S., Mamoon, W.B., Rahman, M.R., 2023. Random forest classifications for landuse mapping to assess rapid flood damage using Sentinel-1 and Sentinel-2 data. Remote. Sens. Appl.: Soc. Environ. 30, 100947. http://dx.doi.org/10.1016/j.rsase.2023.100947.

Breiman, L., 2001. Random forests. Mach. Learn. 45 (1), 5–32. http://dx.doi.org/10.1023/A:1010933404324.

Cahyadi, M.N., Bawasir, A., Arief, S., Widodo, A., Rusli, M., Kusumawardani, D., Rahmawati, Y., Martina, A., Maulida, P., Lestiana, H., 2024. Analysis of the effect of the 2021 Semeru eruption on water vapor content and atmospheric particles using GNSS and remote sensing. Geod. Geodyn. 15 (1), 33–41. http://dx.doi.org/10.1016/j.geog.2023.04.005.

De Zan, F., Monti Guarnieri, A., 2006. TOPSAR: Terrain observation by progressive scans. IEEE Trans. Geosci. Remote Sens. 44 (9), 2352–2360. http://dx.doi.org/10.1109/TGRS.2006.873853.

Du, P., Samat, A., Waske, B., Liu, S., Li, Z., 2015. Random forest and rotation forest for fully polarized SAR image classification using polarimetric and spatial features. ISPRS J. Photogramm. Remote Sens. 105, 38–53. http://dx.doi.org/10.1016/j.isprsjprs.2015.03.002.

Dualeh, E.W., Ebmeier, S.K., Wright, T.J., Albino, F., Naismith, A., Biggs, J., Ordoñez, P.A., Boogher, R.M., Roca, A., 2021. Analyzing explosive volcanic deposits from satellite-based radar backscatter, volcán de fuego, 2018. J. Geophys. Res.: Solid Earth 126 (9), http://dx.doi.org/10.1029/2021JB022250.

Dumaisnil, C., Thouret, J.-C., Chambon, G., Doyle, E.E., Cronin, S., Surono, M., 2010. Hydraulic, physical and rheological characteristics of rain-triggered lahars at Semeru volcano, Indonesia. Earth Surf. Process. Landf. 35 (13), 1573–1590. http://dx.doi.org/10.1002/esp.2003.

Ebmeier, S.K., Biggs, J., Mather, T.A., Amelung, F., 2013. Applicability of insar to tropical volcanoes: insights from central america. Geol. Soc. Lond. Spec. Publ. 380 (1), 15–37. http://dx.doi.org/10.1144/sp380.2.

Ezquerro, P., Bru, G., Galindo, I., Monserrat, O., García-Davalillo, J., Sánchez, N., Montoya, I., Palamà, R., Mateos, R., Pérez-López, R., González-Alonso, E., Grandin, R., Guardiola-Albert, C., López-Vinielles, J., Fernández-Merodo, J., Herrera, G., Béjar-Pizarro, M., 2023. Analysis of SAR-derived products to support emergency management during volcanic crisis: La palma case study. Remote Sens. Environ. 295, 113668. http://dx.doi.org/10.1016/j.rse.2023.113668.

Ferrentino, E., Bignami, C., Nunziata, F., Stramondo, S., Migliaccio, M., 2023. On the ability of dual-polarimetric SAR measurements to observe lava flows under different volcanic environments. Int. J. Appl. Earth Obs. Geoinf. 123, 103471. http://dx.doi.org/10.1016/j.jag.2023.103471.

Freeman, A., 1992. SAR calibration: an overview. IEEE Trans. Geosci. Remote Sens. 30 (6), 1107–1121. http://dx.doi.org/10.1109/36.193786.

Gao, B.-c., 1996. NDWI—A normalized difference water index for remote sensing of vegetation liquid water from space. Remote Sens. Environ. 58 (3), 257–266. http://dx.doi.org/10.1016/s0034-4257(96)00067-3.

Global Volcanism Program, 2022. Report on semeru (Indonesia). In: Crafford, A.E., Venzke, E. (Eds.), Bulletin of the Global Volcanism Network, 47:1. Smithsonian Institution, http://dx.doi.org/10.5479/si.gvp.bgvn202201-263300.

Global Volcanism Program, 2025. Report on semeru (Indonesia). 19 November-25 November 2025. Smithsonian Institution and US Geological Survey.

Goitom, B., Oppenheimer, C., Hammond, J.O.S., Grandin, R., Barnie, T., Donovan, A., Ogubazghi, G., Yohannes, E., Kibrom, G., Kendall, J.-M., Carn, S.A., Fee, D., Sealing, C., Keir, D., Ayele, A., Blundy, J., Hamlyn, J., Wright, T., Berhe, S., 2015. First recorded eruption of Nabro volcano, Eritrea, 2011. Bull. Volcanol. 77 (10), 85. http://dx.doi.org/10.1007/s00445-015-0966-3.

Grémion, S., Pinel, V., Shreve, T., Beauducel, F., Putra, R., Solikhin, A., Santoso, A.B., Humaida, H., 2023. Tracking the evolution of the summit lava dome of merapi volcano between 2018 and 2019 using DEMs derived from TanDEM-X and Pléiades data. J. Volcanol. Geotherm. Res. 433, 107732. http://dx.doi.org/10.1016/j.jvolgeores.2022.107732.

Hendrawan, A., Nabilah, M., Setyadji, B., Sadarviana, V., 2023. Lahar inundation estimation of mount semeru relating to the 4 th December 2021 volcano eruption. IOP Conf. Ser.: Earth Environ. Sci. 1276, 012013. http://dx.doi.org/10.1088/1755-1315/1276/1/012013.

International Federation of Red Cross and Red Crescent Societies, 2022. Indonesia: Mount Semeru Eruption Operation. Technical Report MDRID023.

Irawan, L., Farihah, S., Eko, W., Azizah, V., Hartono, R., Masruroh, H., Mapa, M.T., 2024. The effectivity of community-based early warning system on reducing Semeru eruption impact post-eruption 2021. IOP Conf. Ser.: Earth Environ. Sci. 1314, 012037. http://dx.doi.org/10.1088/1755-1315/1314/1/012037.

Iswari, M.Y., Anggraini, K., 2018. Demnas: model digital ketinggian nasional UntUk Aplikasi kepesisiran. OSEANA 43 (4), http://dx.doi.org/10.14203/oseana.2018.vol.43no.4.2.

Joyce, K., Samsonov, S., Manville, V., Jongens, R., Graettinger, A., Cronin, S., 2009. Remote sensing data types and techniques for lahar path detection: A case study at Mt Ruapehu, New Zealand. Remote Sens. Environ. 113, 1778–1786. http://dx.doi.org/10.1016/j.rse.2009.04.001.

Julzarika, A., Harintaka, 2019. Indonesian DEMNAS: DSM or DTM? In: 2019 IEEE Asia-Pacific Conference on Geoscience, Electronics and Remote Sensing Technology (AGERS). pp. 31–36. http://dx.doi.org/10.1109/AGERS48446.2019.9034351.

Kellndorfer, J., Flores-Anderson, A., Herndon, K., Thapa, R., 2019. Chapter 3: Using SAR data for mapping deforestation and forest degradation. In: The SAR Handbook. Comprehensive Methodologies for Forest Monitoring and Biomass Estimation. pp. 65–79. http://dx.doi.org/10.25966/68c9-gw82.

Kerle, N., Oppenheimer, C., 2002. Satellite remote sensing as a tool in lahar disaster management. Disasters 26 (2), 140–160. http://dx.doi.org/10.1111/1467-7717.00197.

Kristianto, Basuki, A., Purnamasari, H.D., Syahbana, D.K., 2023. The 2021 Semeru volcano eruption: An insight from visual, seismic, and deformation monitoring data. IOP Conf. Ser.: Earth Environ. Sci. 1227 (1), 012030. http://dx.doi.org/10.1088/1755-1315/1227/1/012030.

Kubanek, J., Westerhaus, M., Schenk, A., Aisyah, N., Brotopuspito, K.S., Heck, B., 2015. Volumetric change quantification of the 2010 Merapi eruption using TanDEM-X InSAR. Remote Sens. Environ. 164, 16–25. http://dx.doi.org/10.1016/j.rse.2015.02.027.

Kurnianto, F.A., Naim, M., Susiati, A., Susanti, D.A.J., 2024. Insight into the 2021 semeru volcano eruption from rapid monitoring of its pyroclastic deposits using google earth engine and multi-sensor data. Remote. Sens. Appl.: Soc. Environ. 36, 101380.. http://dx.doi.org/10.1016/j.rsase.2024.101380.

Lee, J.-Y., Jung, S.-W., Hong, S.-H., 2023. Mapping lava flow from the Kilauea eruption of 2018 in the east rift zone using space-based synthetic aperture radar. GIScience Remote. Sens. 60 (1), 2176275. http://dx.doi.org/10.1080/15481603.2023.2176275.

Lee, J., Kim, K., Lee, K., 2024. Multi-sensor image classification using the random forest algorithm in google earth engine with KOMPSAT-3/5 and CAS500-1 images. Remote. Sens. 16 (24), http://dx.doi.org/10.3390/rs16244622.

Lundgren, P., Nikkhoo, M., Samsonov, S.V., Milillo, P., Gil-Cruz, F., Lazo, J., 2017. Source model for the Copahue volcano magma plumbing system constrained by InSAR surface deformation observations. J. Geophys. Res.: Solid Earth 122 (7), 5729–5747. http://dx.doi.org/10.1002/2017JB014368.

Macorps, E., Jo, M., Osmanoglu, B., Albayrak, R.A., 2023. Mapping areas impacted by volcanic flows during an eruption using synthetic aperture radar and optical imagery. Int. Arch. Photogramm. Remote. Sens. Spat. Inf. Sci. XLVIII-M-1-2023, 175–182. http://dx.doi.org/10.5194/isprs-archives-XLVIII-M-1-2023-175-2023.

McAlpin, D., Meyer, F.J., 2013. Multi-sensor data fusion for remote sensing of post-eruptive deformation and depositional features at redoubt volcano. 2009 Erupt. Redoubt Volcano, Alsk. 259, 414–423. http://dx.doi.org/10.1016/j.jvolgeores.2012.08.006.

Meyer, F.J., 2019. CHAPTER 2 spaceborne synthetic aperture radar : Principles , data access , and basic processing techniques.

Meyer, F., McAlpin, D., Gong, W., Ajadi, O., Arko, S., Webley, P., Dehn, J., 2015. Integrating SAR and derived products into operational volcano monitoring and decision support systems. High-Resolution Earth Imaging Geospatial Inf. 100, 106–117. http://dx.doi.org/10.1016/j.isprsjprs.2014.05.009.

Orynbaikyzy, A., Plank, S., Vetrita, Y., Martinis, S., Santoso, I., Dwi Ismanto, R., Chusnayah, F., Tjahjaningsih, A., Suwarsono, Genzano, N., Marchese, F., Rokhis Khomarudin, M., Strunz, G., 2023. Joint use of Sentinel-2 and sentinel-1 data for rapid mapping of volcanic eruption deposits in Southeast Asia. Int. J. Appl. Earth Obs. Geoinf. 116, 103166. http://dx.doi.org/10.1016/j.jag.2022.103166.

Orynbaikyzy, A., Santoso, I., Rösch, M., Martinis, S., Ismanto, R.D., Vetrita, Y., Khomarudin, M., Strunz, G., Plank, S., 2025. Land surface change detection after major volcanic eruptions in Indonesia using machine learning and spatial-temporal transferability. Int. J. Appl. Earth Obs. Geoinf. 145, 104965. http://dx.doi.org/10.1016/j.jag.2025.104965.

Pallister, J.S., Schneider, D.J., Griswold, J.P., Keeler, R.H., Burton, W.C., Noyles, C., Newhall, C.G., Ratdomopurbo, A., 2013. Merapi 2010 eruption—Chronology and extrusion rates monitored with satellite radar and used in eruption forecasting. Merapi Erupt. 261, 144–152. http://dx.doi.org/10.1016/j.jvolgeores.2012.07.012.

Pepe, A., Calò, F., 2017. A review of interferometric synthetic aperture RADAR (InSAR) multi-track approaches for the retrieval of earth's surface displacements. Appl. Sci. 7 (12), http://dx.doi.org/10.3390/app7121264.

Perwita, C., Aprilia, F., Maryanto, S., Arrasyid, H., Tsabitah, A., 2023. Hazards mitigation of lahar flows on semeru volcano after the 4 December 2021 eruption based on PS-InSAR. Int. J. Disaster Manag. 5 (3), 193–202. http://dx.doi.org/10.24815/ijdm.v5i3.29098.

Pettorelli, N., 2013. The Normalized Difference Vegetation Index. Oxford University Press, http://dx.doi.org/10.1093/acprof:osobl/9780199693160.001.0001.

Phan, H., Le Toan, T., Bouvet, A., 2021. Understanding dense time series of sentinel-1 backscatter from rice fields: Case study in a province of the mekong delta, Vietnam. Remote. Sens. 13, 921. http://dx.doi.org/10.3390/rs13050921.

Poland, M.P., 2022. Synthetic aperture radar volcanic flow maps (SAR VFMs): a simple method for rapid identification and mapping of volcanic mass flows. Bull. Volcanol. 84 (3), 32. http://dx.doi.org/10.1007/s00445-022-01539-7.

Popescu, R., Anantrasirichai, N., Biggs, J., 2025. Unsupervised anomaly detection for volcanic deformation in InSAR imagery. Earth Space Sci. 12 (6), http://dx.doi.org/10.1029/2024EA003892, e2024EA003892.

Procter, J., Zernack, A., Mead, S., Morgan, M., Cronin, S., 2021. A review of lahars; past deposits, historic events and present-day simulations from Mt. Ruapehu and Mt. Taranaki, New Zealand. N. Z. J. Geol. Geophys. 64 (2–3), 479–503. http://dx.doi.org/10.1080/00288306.2020.1824999.

Richardson, A.J., Wiegand, C., 1977. Distinguishing vegetation from soil background information. Photogramm. Eng. Remote Sens. 43 (12), 1541–1552.

Roy, D.P., Huang, H., Houborg, R., Martins, V.S., 2021. A global analysis of the temporal availability of PlanetScope high spatial resolution multi-spectral imagery. Remote Sens. Environ. 264, 112586. http://dx.doi.org/10.1016/j.rse.2021.112586.

Rozaki, Z., Rahmawati, N., Relawati, R., Wijaya, O., Rahayu, L., Triyono, Azizah, S.N., Rahmat, A., Jumakir, 2022. Strategies for overcoming farmers' lives in volcano-prone areas: A case study in mount semeru, Indonesia. 7, (1), pp. 486–503. http://dx.doi.org/10.1515/opag-2022-0118.

Schilling, S.P., 2014. Laharz_py: GIS Tools for Automated Mapping of Lahar Inundation Hazard Zones. Report 2014–1073, Reston, VA, p. 82. http://dx.doi.org/10.3133/ofr20141073.

Shih, P., Liu, C., 2005. Comparative assessment of content-based face image retrieval in different color spaces. Int. J. Pattern Recognit. Artif. Intell. 19 (07), 873–893. http://dx.doi.org/10.1142/S0218001405004381.

Shoji, S., Takahashi, T., 2002. Environmental and agricultural significance of volcanic ash soils. Glob. Environ. Res. 6.

Siswowidjoyo, S., Sudarsono, U., Wirakusumah, A., 1997. The threat of hazards in the semeru volcano region ineast java, Indonesia. J. Asian Earth Sci. 15 (2), 185–194. http://dx.doi.org/10.1016/S0743-9547(97)00007-X.

Small, D., 2011. Flattening Gamma: Radiometric terrain correction for SAR imagery. IEEE Trans. Geosci. Remote Sens. 49 (8), 3081–3093. http://dx.doi.org/10.1109/TGRS.2011.2120616.

Solikhin, A., Pinel, V., Vandemeulebrouck, J., Thouret, J.-C., Hendrasto, M., 2015a. Mapping the 2010 merapi pyroclastic deposits using dual-polarization synthetic aperture radar (SAR) data. Remote Sens. Environ. 158, 180–192. http://dx.doi.org/10.1016/j.rse.2014.11.002.

Solikhin, A., Thouret, J.-C., Liew, S.C., Gupta, A., Sayudi, D.S., Oehler, J.-F., Kassouk, Z., 2015b. High-spatial-resolution imagery helps map deposits of the large (VEI 4) 2010 merapi volcano eruption and their impact. Bull. Volcanol. 77 (3), 20. http://dx.doi.org/10.1007/s00445-015-0908-0.

Soudani, K., Delpierre, N., Berveiller, D., Hmimina, G., Vincent, G., Morfin, A., Dufrêne, É., 2021. Potential of C-band synthetic aperture radar sentinel-1 time-series for the monitoring of phenological cycles in a deciduous forest. Int. J. Appl. Earth Obs. Geoinf. 104, 102505. http://dx.doi.org/10.1016/j.jag.2021.102505.

Suhadha, A.G., Harintaka, H., 2024. Multidimensional displacement analysis of semeru volcano, Indonesia following december 2021 eruption from multitrack insar observation. Earth Sci. Informatics 17 (2), 1539–1552. http://dx.doi.org/10.1007/s12145-024-01248-z.

Suhendro, I., Gurusinga, M.A., Toramaru, A., Harijoko, A., Wibowo, H.E., Latief, G.A.E.-Z., Priyana, P.E., Suhartono, M.A.T.S.P., Rahmawati, Z.Y., 2025. Magma ascent dynamics and transport process of the mt. semeru lava dome that collapsed on 4th december 2021 (east java, Indonesia). J. Volcanol. Geotherm. Res. 467, 108432. http://dx.doi.org/10.1016/j.jvolgeores.2025.108432.

Tan, B., Wolfe, R., Lin, G., 2021. PlanetScope imagery geolocation accuracy assessment. In: AGU Fall Meeting Abstracts. In: AGU Fall Meeting Abstracts, 2021, pp. B15I–1545.

Thouret, J.-C., Lavigne, F., Suwa, H., Sukatja, B., Surono, 2007. Volcanic hazards at mount semeru, east java (Indonesia), with emphasis on lahars. Bull. Volcanol. 70 (2), 221–244. http://dx.doi.org/10.1007/s00445-007-0133-6.

Verhoest, N.E., Lievens, H., Wagner, W., Álvarez-Mozos, J., Moran, M.S., Mattia, F., 2008. On the soil roughness parameterization problem in soil moisture retrieval of bare surfaces from synthetic aperture radar. Sensors 8 (7), 4213–4248. http://dx.doi.org/10.3390/s8074213.

Wadge, G., Cole, P., Stinton, A., Komorowski, J.-C., Stewart, R., Toombs, A., Legendre, Y., 2011. Rapid topographic change measured by high-resolution satellite radar at soufriere hills volcano, montserrat, 2008–2010. J. Volcanol. Geotherm. Res. 199 (1), 142–152. http://dx.doi.org/10.1016/j.jvolgeores.2010.10.011.

Wadge, G., Scheuchl, B., Stevens, N.F., 2002. Spaceborne radar measurements of the eruption of Soufrière Hills Volcano, Montserrat. Geol. Soc. Lond. Memoirs 21 (1), 583–594. http://dx.doi.org/10.1144/gsl.mem.2002.021.01.27.

Wahyuningtyas, N., YANIAFARI, R., Rosyida, F., Megasari, R., Dewi, K., Khotimah, K., 2021. Mapping a eruption disaster-prone area in the bromo-tengger-semeru national tourism strategic area (case study of Mount Semeru, Indonesia). GeoJournal Tour. Geosites 39, 1430–1438. http://dx.doi.org/10.30892/gtg.394spl14-787.

Waitt, R.B., 2013. Lahar. In: Bobrowsky, P.T. (Ed.), Encyclopedia of Natural Hazards. Springer Netherlands, Dordrecht, pp. 579–580. http://dx.doi.org/10.1007/978-1-4020-4399-4_206.

Wang, T., Poland, M.P., Lu, Z., 2015. Dome growth at mount cleveland, aleutian arc, quantified by time series TerraSAR-x imagery. Geophys. Res. Lett. 42 (24), 10,614–10,621. http://dx.doi.org/10.1002/2015GL066784.

Wang, Z., Zhang, F., Wu, C., Xia, J., 2024. Rapid mapping of volcanic eruption building damage: A model based on prior knowledge and few-shot fine-tuning. Int. J. Appl. Earth Obs. Geoinf. 126, 103622. http://dx.doi.org/10.1016/j.jag.2023.103622.

Wei, L., Sun, Y., Pan, X., Liu, G., Trasatti, E., Tolomei, C., Ventura, G., Bignami, C., Ao, M., Liu, S., 2024. Dynamics of the 2021 unrest at changbaishan tianchi volcano from ALOS-2/PALSAR-2 and seismic data. Int. J. Appl. Earth Obs. Geoinf. 128, 103775. http://dx.doi.org/10.1016/j.jag.2024.103775.